JOURNAL OF GEOPHYSICAL RESEARCH, VOL. 114, F01003, doi:10.1029/2007JF000970, 2009

Coherent flow structures in a depth-limited flow over a gravel surface: The role of near-bed turbulence and influence of Reynolds number

Richard J. Hardy,[1] James L. Best,[2] Stuart N. Lane,[1] and Patrice E. Carbonneau[1]

Received 18 December 2007; revised 18 August 2008; accepted 1 October 2008; published 10 January 2009.

[1] In gravel bed rivers, the microtopography of the bed exerts a significant effect on the generation of turbulent flow structures. Although field and laboratory measurements have indicated that flows over gravel beds contain coherent macroturbulent flow structures, the origin of these phenomena, and their relationship to the ensemble of individual roughness elements forming the bed, is not quantitatively well understood. Here we report upon a flume experiment in which flow over a gravel surface is quantified through the application of digital particle imaging velocimetry, which allows study of the downstream and vertical components of velocity over the entire flow field. The results indicate that as the Reynolds number increases (1) the visual distinctiveness of the coherent flow structures becomes more defined, (2) the upstream slope of the structures increases, and (3) the turbulence intensity of the structures increases. Analysis of the mean velocity components, the turbulence intensity, and the flow structure using quadrant analysis demonstrates that these large-scale turbulent structures originate from flow interactions with the bed topography. Detection of the dominant temporal length scales through wavelet analysis enables calculation of mean separation zone lengths associated with the gravel roughness through standard scaling laws. The calculated separation zone lengths demonstrate that wake flapping is a dominant mechanism in the production of large-scale coherent flow structures in gravel bed rivers. Thus, we show that coherent flow structures over gravels owe their origin to bed-generated turbulence and that large-scale outer layer structures are the result of flow-topography interactions in the near-bed region associated with wake flapping.

Citation: Hardy, R. J., J. L. Best, S. N. Lane, and P. E. Carbonneau (2009), Coherent flow structures in a depth-limited flow over a gravel surface: The role of near-bed turbulence and influence of Reynolds number, *J. Geophys. Res.*, *114*, F01003, doi:10.1029/2007JF000970.

1. Introduction

[2] Gravel bed rivers have complex, porous and irregular surfaces [*Robert et al.*, 1992; *Kirchner et al.*, 1990; *Clifford et al.*, 1992; *Butler et al.*, 2002; *Lane et al.*, 2004] characterized by a range of morphological forms. These forms scale from individual gravel grains through microtopographic particle clusters to large-scale bed forms [*Brayshaw et al.*, 1983; *Robert et al.*, 1993]. Flow in gravel bed rivers is typically shallow, and the relative submergence of clasts (ratio of mean flow depth to typical roughness height) seldom exceeds 10–20 in floods and can be less than 5 during base flow conditions. In such shallow flows, the microtopography of the bed exerts a significant influence on the generation of coherent flow structures [*Wiberg and Smith*, 1991; *Dinehart*, 1992]. Such structures are related to the wakes of individual obstacle clasts, and jetting of higher-velocity flow between such clasts, and may not penetrate vertically within the flow to much above the tops of the obstacles. Yet, field measurements and laboratory visualization also indicate that shallow flows over gravel beds contain coherent macroturbulent flow structures [e.g., *Kirkbride*, 1993; *Best et al.*, 2001; *Roy et al.*, 2004], whose origin and relationship to the ensemble of individual roughness elements forming the bed is not quantitatively well understood. Much of the uncertainty in our understanding of these flow structures stems from the fact that most previous studies have used point time series, sometimes with many points, but not time series of the whole flow field. Here we investigate the nature of coherent flow structures formed over heterogeneous gravel surfaces and how these are influenced by flow Reynolds number, as dictated by changing the mean flow velocity while keeping the flow depth constant. These aims are addressed by use of digital particle imaging velocimetry (DPIV), which enables the whole, time-dependent flow field to be examined.

2. Background

[3] Coherent turbulent flow structures, defined herein as repetitive quasi-cyclic large-scale turbulent motions [*Shvidchenko and Pender*, 2001], are prevalent in depth-

[1]Department of Geography, Durham University, Durham, UK.
[2]Department of Geology and Department of Geography, and Ven Te Chow Hydrosystems Laboratory, University of Illinois at Urbana-Champaign, Urbana, Illinois, USA.

0148-0227/09/2007JF000970$09.00

limited open channel flows. *Shvidchenko and Pender* [2001] report that *Velikanov* [1949] was the first to propose a theoretical model of turbulence in open channels that consisted of depth-scale rolling vortices that were both structured and quasiperiodic. Since then, several experimental studies have combined flow visualization techniques with flow measurements [e.g., *Fidman*, 1953, 1991; *Klaven*, 1966; *Klaven and Kopaliani*, 1973; *Imamoto and Ishigaki*, 1986a, 1986b; *Best et al.*, 2001; *Shvidchenko and Pender*, 2001; *Roy et al.*, 2004] to gain an understanding of the generation, evolution and dissipation of these large-scale structures, over both smooth and homogenous rough surfaces. These studies have identified large-scale eddies that scale closely with the flow depth (h) in the vertical and approximately $2h$ in the lateral spanwise direction [*Zaitsev*, 1984]. The downstream scale of these structures appears to be dependent upon both bed roughness and hydraulic conditions: the greater the flow depth and velocity, the more pronounced the development of the coherent flow structure [*Shvidchenko and Pender*, 2001]. The downstream scale of these structures has been proposed to be between $4h$ and $7h$, with this scale increasing as bed roughness decreases [*Klaven*, 1966; *Klaven and Kopaliani*, 1973; *Shvidchenko and Pender*, 2001]. It has also been suggested that the origin of these flow structures is closely linked to the bursting phenomena in turbulent boundary layers [*Grishanin*, 1990; *Yalin*, 1992; *Smith*, 1996; *Grass and Mansour-Tehrani*, 1996] where (1) ejected, low-momentum fluid travels across the entire flow depth irrespective of the bed roughness [*Grass*, 1971; *Talmon et al.*, 1986*; Shen and Lemmin*, 1999] and (2) high-momentum fluid moves from near the water surface toward the bed [*Rashidi and Banerjee*, 1988; *Grass et al.*, 1991]. However, in most physical modeling studies, the rough boundaries have been restricted to well-sorted beds composed of homogenous particles where skimming flow develops [*Grass*, 1971; *Grass et al.*, 1991; *Krogstad et al.*, 1992]. Therein, the mechanism of momentum exchange shows strong similarities to bursting processes over smooth surfaces [*Smith*, 1996; *Grass and Mansour-Tehrani*, 1996], although the origin of such structures may be radically different [*Kirkbride*, 1993; *Smith*, 1996; *Best*, 1996]. Studies of turbulent flow structures in gravel bed rivers in the field are limited because of the challenges of instrumentation [*Roy et al.*, 1996], although studies over natural gravel beds suggest that coherent flow structures in the near-bed region scale with respect to both the size and sorting of the bed material [*Clifford et al.*, 1992; *Clifford and French*, 1993]. As with flow over smooth beds, the larger structures may be created by the coalescence and amalgamation of numerous smaller-scale structures [*Head and Bandyopadhyay*, 1981; *Smith et al.*, 1991]. Microtopographic features, such as particle clusters, are prevalent in most gravel bed rivers [*Brayshaw et al.*, 1983; *Biggs et al.*, 1997] and localized topographic forcing of flow may provide a dominant mechanism for momentum exchange. This is commonly thought to be in the form of a horseshoe vortex formed upstream of clasts, and shedding of vortices in the lee of the cluster [*Robert et al.*, 1992, 1993; *Kirkbride*, 1993], with the upstream horseshoe vortex being analogous to a simple juncture vortex [*Brayshaw et al.*, 1983; *Best*, 1996; *Buffin-Bélanger and Roy*, 1998; *Lawless and Robert*, 2001]. Here, a region of weak recirculation is caused by flow stagnation and separation immediately upstream of the object, which leads to the generation of vorticity that can, in turn, trigger the formation of large-scale coherent flow structures [*Lawless*, 2004].

[4] Given the above, it is clear that a full understanding of the causes and regularity of macroturbulent fluctuations in shallow flows over gravel beds does not exist. Indeed, process information derived from data collected from previous studies provides contradictory evidence. Some studies have been interpreted as showing low-frequency velocity fluctuations corresponding to a spatial scale of the order of the flow depth [*Komori et al.*, 1982; *Grinvald and Nikora*, 1988; *Clifford et al.*, 1992; *Lapointe*, 1992; *Nezu and Nakagawa*, 1993; *Robert et al.*, 1993; *Roy et al.*, 1996; *Cellino and Graf*, 1999; *Shen and Lemmin*, 1999]. However, other authors do not detect any regular periodicity in the turbulent fluctuations of flow [*Grinvald*, 1974; *Nikora and Smart*, 1997], which suggests the coherent flow structures are randomly distributed in time and space [*Nychas et al.*, 1973; *Smith*, 1996; *Nikora and Goring*, 1999]. In order to determine quantitatively the generation, evolution and typical spatial and temporal persistence of such turbulent flow structures over heterogeneous gravel surfaces, it is necessary both to visualize and quantify the whole flow field continuously. The present paper reports on a study of depth-limited flow at three different flow Reynolds numbers over a water-worked gravel surface. The influence of the Reynolds number was investigated by increasing the mean flow velocity while keeping flow depth constant. Flow velocities were quantified by application of two-dimensional digital particle imaging velocimetry (2-D DPIV) which enables continuous measurement of the whole flow field. These DPIV measurements were linked to high-resolution quantification of the bed surface topography obtained using digital photogrammetry. This experimental setup enabled study of the generation and evolution of coherent flow structures over a known bed topography that allowed identification of (1) the topographic characteristics required for generation of macroscale turbulent flow structures, (2) the geometric shape of the flow structures, (3) the temporal length scales of the flow structures, and (4) how these characteristics change with flow Reynolds number.

3. Experimental Methodology

[5] All experiments were conducted in a hydraulic flume, 10 m in length (l_c) and 0.3 m in width (w). A series of four "honeycomb" baffle plates were fastened to the channel inlet in order to dampen incoming turbulence and to help establish a uniform, subcritical, depth-limited boundary layer upstream of the gravel surface. The slope of the flume was adjusted to achieve constant flow depth within the test section, which was located 5.5 m downstream from the channel inlet.

3.1. Digital Elevation Model Generation Using Digital Photogrammetry

[6] A bulk sample of sediment from the River Wharfe, northern England, was placed in the flume and water worked until a stable bed (no sediment transport) was obtained. The surface morphology was then measured using close range terrestrial digital photogrammetry. Using the methods established by *Butler et al.* [1998] and *Carbonneau*

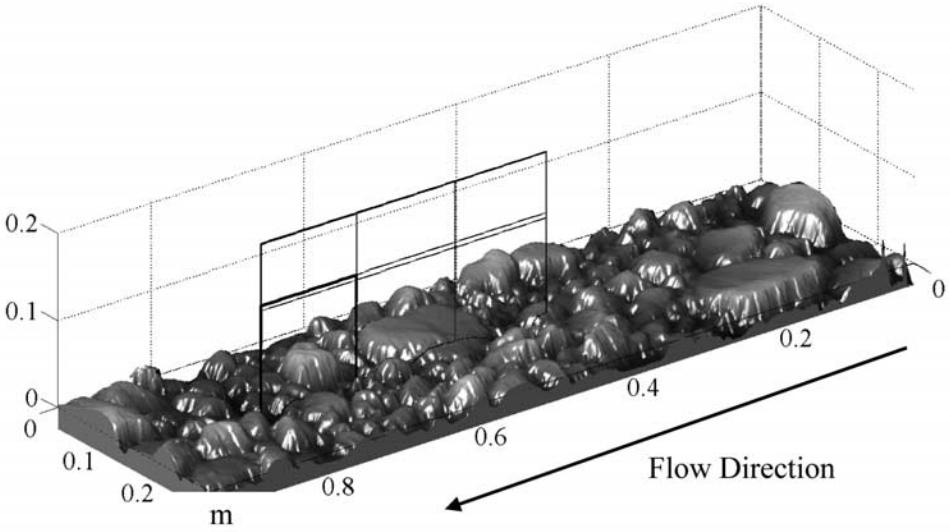

Figure 1. The digital elevation model measured by digital photogrammetry on a 1 mm × 1 mm resolution. The boxes represent the interrogation regions of the digital particle imaging velocimetry with an area of 0.25 m × 0.252 m. The bold box on the left-hand side of the image demonstrates the flow field region investigated herein.

et al. [2003], a photogrammetric survey was designed in order to produce digital elevation models (DEMs) with a spatial resolution of 1 mm^2. This survey employed a Kodak DCS 460 digital camera with an imaging resolution of 3060 × 2036 pixels in standard red, green and blue bands. High-precision DEMs are regularly produced with such cameras provided that additional surveyed ground calibration points are added on the target surface [*Carbonneau et al.*, 2003]. Accordingly, 84 ground control targets were glued to stable large clasts in the bed. These targets were then surveyed with a Geodimeter 608S total station to obtain x, y, z coordinates of points with a known position in the imagery. To generate a DEM of the investigation region, nine consecutive images with 60% overlap between consecutive images were required. The resulting DEM was not smoothed. However, the edges were cropped to eliminate errors that typically occur on the periphery of the DEM, as a result of greater geometric distortion with distance away from the image centre. The size of the final DEM was 0.923 by 0.26 m (Figure 1) with a vertical precision of ±0.001 m. The topographic statistics of the DEM are given in Table 1, and represent the topographic elevation of each 0.001 m grid cell rather than that of individual gravel particles.

3.2. Hydraulic Conditions

[7] In these experiments, the water depth was maintained at a constant value of 0.2 m, with three different experiments being undertaken at mean downstream velocities at 0.4 z/h of 0.155 m s^{-1}, 0.3 m s^{-1}, and 0.435 m s^{-1} (where z and h are height above the bed and flow depth, respectively). The constant flow depth of 0.2 m was adopted for both theoretical and practical reasons. The present study aimed to understand the nature of coherent flow structures forming over a heterogeneous gravel surface and the influence of an increase in flow Reynolds number (through changes in flow velocity) upon the generation of these flow structures. Consequently, depth was held constant and mean flow velocity was used to increase the flow Reynolds number. Additionally, in practical terms, it was not possible to illuminate the whole flow depth with the laser configuration used herein. If greater flow depths were used it would not have been possible to track the flow structures to the water surface. Table 2 summarizes the hydraulic conditions used in the study and the experiments are subsequently referred to according to their flow Reynolds numbers (Re).

[8] Velocity measurements were obtained using a DANTEC two-dimensional digital particle imaging velocimetry system (2-D DPIV), which is a nonintrusive, whole flow field technique for velocity measurement. A major advantage of DPIV is that it is multipoint, and can be used to study the entire flow field instantaneously to allow quantitative flow visualization (by analysis of consecutive resolved velocity images) where flow structures can be observed moving over the bed. The DPIV methodology and postprocessing applied herein is identical to that previously used by *Hardy et al.* [2005] and only a brief synopsis

Table 1. Topographic Statistics of the Digital Elevation Model

	Particle Size (m)	Roughness Height
Mean	0.0236	0.1179
σ	0.0086	...
D_{16}	0.0150	0.0748
D_{50}	0.0226	0.1130
D_{84}	0.0329	0.1646

Table 2. Hydraulic Conditions Used in This Analysis

	Experiment 1	Experiment 2	Experiment 3
Flow velocity (m s^{-1})	0.155	0.300	0.435
Flow depth (m)	0.200	0.200	0.200
Q_s (m^3 s^{-1})	9.3×10^{-3}	1.8×10^{-2}	2.6×10^{-2}
Froude number	~0.11	~0.21	~0.31
Reynolds number	~13,000	~25,000	~37,000

is provided below. Measurement is based upon seeding the flow with neutrally buoyant tracer particles (hollow reflective glass spheres with a mean diameter of 10 μm) and illuminating the flow field with a double-pulsed 50 mJ Nd-YAG laser light sheet, with the time gap between flashes being set to 0.067 s. When the laser sheet illuminated the flow, light was scattered by the seeding material and detected by a charge-coupled device (CCD) camera positioned perpendicular to the light sheet. In order to derive a velocity vector map, a digital mesh of small interrogation regions (16 $\times$ 16 pixels, where 1 pixel $\approx 2.5 \times 10^{-4}$ m) was draped over the images. For each interrogation region, in each pair of images, the displacement of groups of particles between the first and second image was measured using a fast Fourier transform–based spatial cross-correlation technique and a velocity vector was determined [see *Westerweel*, 1997]. The entire process was repeated at 15 Hz until the flow was sampled for 1 min. This sample length provided a sufficient time period to obtain a stationary time series, which was tested by systematic convergence of the cumulative variance for both velocity components to a constant value (for a full explanation see *Sukhodolov and Rhoads* [2001]) and follows the recommended sampling period suggested by *Buffin-Bélanger and Roy* [2005].

[9] In the present study, the DPIV camera was located perpendicular to the bed, so that slices of flow could be interrogated for the downstream u and vertical w components of velocity. With a 16 $\times$ 16 pixel interrogation region and the setup described above, each instantaneous velocity map consisted of 15,750 individual vectors enabling data collection at a spatial resolution of 2×10^{-3} m. In order to maximize the signal-to-noise ratio of the particle cross correlations, a sequence of six quality checks [see *Hardy et al.*, 2005] was undertaken. With this methodology, the estimated precision of the derived velocities is greater than one tenth of a pixel [*Wilbert and Gharib*, 1991; *Huang et al.*, 1997; *DANTEC Dynamics*, 2000]. Thus, the uncertainty in the velocity measurement is better than ± 0.08 mm s^{-1}.

[10] The area illuminated by the light sheet over the gravel surfaces was aligned along the centerline of the flume. For this transect, three sections, each $\simeq$0.25 m in downstream length, were collected to enable a time-averaged map of 0.75 m length to be quantified (see location of DPIV area in Figure 1). Because of the illumination requirements, two regions needed to be illuminated and DPIV data collected in the vertical dimension: (1) the near-bed region and (2) the region extending to the free surface (see Figure 1). Thus, six interrogation regions were collected to cover the 0.75 m downstream length for each of the three different flow conditions, with the map for each Reynolds number consisting of $\sim$90,000 points.

3.3. Analysis Methodology

[11] The DPIV data was collected on a regular grid (125 $\times$ 126, covering a spatial area of 0.25 by 0.252 m) with each point providing a time series for 1 min at a temporal resolution of 15 Hz. The whole flow field can then be analyzed by either time-averaged or time-dependent techniques. In this study, we explore the flow characteristics through (1) the time-averaged flow fields, (2) instantaneous flow visualization, which is achieved by the analysis of consecutive images of the calculated u component velocity minus 0.85 of the mean value at each point following the recommendation of *Adrian et al.* [2000], (3) the time-averaged and instantaneous uw vorticity (ω), (4) the root-mean-square (RMS) values of the deviatoric components of velocity, (5) analysis of turbulent structures through classical quadrant analysis, and (6) identification of temporal length scales through wavelet analysis.

3.3.1. Quadrant Analysis

[12] Quadrant analysis has previously been used to discriminate boundary layer turbulent events by examining the instantaneous deviations of velocity from the mean values [e.g., *Lu and Willmarth*, 1973; *Bogard and Tiederman*, 1986; *Bennett and Best*, 1995; *Hardy et al.*, 2007]. By applying the standard definition of *Lu and Willmarth* [1973], four quadrants can be defined around a zero mean: quadrant 1 events or outward interactions (positive u component, positive w component), quadrant 2 events or ejections (bursts) (negative u component, positive w component), quadrant 3 events or inward interactions (negative u component, negative w component), and quadrant 4 events or inrushes (sweeps) (positive u component, negative w component). In the present analysis, each velocity pair was studied using a "hole" size [*Lu and Willmarth*, 1973; *Bogard and Tiederman*, 1986; *Bennett and Best*, 1995] of one standard deviation, in which the signal was examined only if the values exceeded this threshold.

3.3.2. Wavelet Analysis

[13] Wavelet analysis was identified as the most beneficial method of analysis because visual inspection of the time series suggested that (1) the scales of variability were only intermittently present and (2) the scales of variability evolved temporally and spatially as a function of time (or space). As the evolution of scales of variability is continuous within discrete subseries, one option was to use a windowed Fourier transform. However, this is both inaccurate (as it can result in the aliasing of high- and low-frequency components that do not fall within the frequency range of the window) and inefficient (as a result of the number of frequencies which must be analyzed at each time step regardless of the window size or dominant frequencies present) [*Torrence and Compo*, 1998]. Here, we use wavelet analysis with scale-dependent time frequency localization [e.g., *Labat et al.*, 2000; *Torrence and Compo*, 1998], which is achieved by breaking the data series into a set of scaled and translated versions of a wavelet function, with the scale of the wavelet varying with frequency. Thus, whereas a Fourier transform yields a power value for each frequency determined, wavelet analysis produces power values for a set of locations in time and for a range of frequencies, the latter being related to the scales of the wavelet function considered. Wavelet analysis has also been previously applied in studies of turbulence [e.g., *Farge*, 1992].

[14] A full review of wavelet analysis is provided by *Torrence and Compo* [1998], and the details below are restricted to the application of wavelet analysis in the present study. Herein, we use a simple, real and nonorthogonal wavelet, the Morlet wavelet, to estimate the power present in the time series for a set of s (time) scales of variability and at a set of t time periods. The result is a wavelet power spectrum with power mapped onto each (s, t) location. Choosing the right type of wavelet for a given data series is important, although if the prime goal of the study is

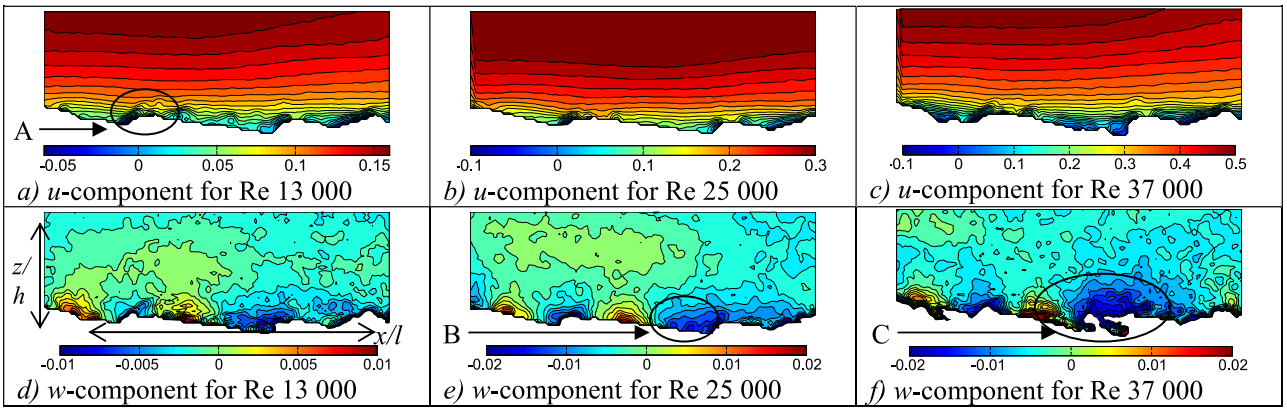

Figure 2. Time-averaged velocity for (a, b, c) the downstream u component and (d, e, f) the vertical w component and for three Reynolds numbers: 13,000 (Figures 2a and 2d), 25,000 (Figures 2b and 2e), and 37,000 (Figures 2c and 2f). Flow direction is from right to left; z/h is equal to 0.12 m, and x/l is equal to 0.25 m. Regions A, B, and C represent areas of local recirculation. All scales are in m s^{-1}.

determination of the wavelet power spectra, the precise choice of the wavelet should not matter as different wavelets will give the same qualitative results [*Torrence and Compo*, 1998]. Indeed, in a global sense, having to choose a particular waveform is no different to the type of assumption made in conventional spectral analysis about the fit of particular waveforms to the data. Nonetheless, some justification of the choice adopted herein is required. First, the prime aim of this analysis was a continuous transformation of the time series into a time-dependent, period frequency series in order to identify the intermittent presence of features at a range of time scales, as well as possible evolution of the scale of features as a function of time. This suggested that the continuous wavelet transform was most appropriate. Second, we should expect a quasi-continuous variation in velocity fluctuations in this time series, and thus a simple wavelet form was most appropriate. Third, we needed to use a wavelet with a good frequency resolution: the data were collected at 15 Hz, leading to the probability of some redundancy at smaller time steps in relation to understanding the characteristics of macroturbulence. Thus, time resolution was less important. As a result of these deliberations, the present analysis utilized a Morlet wavelet, primarily because, of all the simple wavelets considered, it has one of the best resolutions in frequency space. Furthermore, if the schematic diagram of the elementary decomposition of turbulent energy from a characteristic eddy (as proposed by *Tennekes and Lumley* [1972]) is studied, its morphology is very similar to the Morlet wavelet. Consequently, it has been suggested that the Morlet wavelet is the most appropriate for studying the dynamics of turbulence [*Liandrat and Moret-Bailly*, 1990].

[15] Four additional issues need specific mention: (1) the reduction in the reliability of the analysis at the edges of the data series, (2) the scales that will be analyzed, (3) conversion from wavelet scale to Fourier period, and (4) statistical significance testing in relation to the difference between the observed wavelet fits and the theoretical wavelet fits associated with a background spectrum. First, as the edges of a time series are reached, the length (in seconds) of the wavelet that can be resolved will be reduced, and a cone of influence (or detectable scales) needs to be set. The Morlet wavelet has an e-folding time of $\sqrt{2}s$, which was used to set the cone of influence. Second, with hundreds of data at a 15 Hz resolution, there are 999 possible scales of analysis. It is inefficient to analyze all of these scales as this leads to redundancy in power determination at long scales (where the resolved scale has a much lower frequency than 15 Hz) and poor resolution at short scales (where the resolved scale has a frequency approaching the Nyquist frequency of 7.5 Hz). Thus, we initially used a dyadic series and analyzed over the range 2^9 scales, which corresponds to scales of up to 51.2 s, but constrained by the cone of influence at the edges. In order to obtain a reasonable resolution in frequency space between dyadic numbers, tests suggested an increment of 0.1 was appropriate. Thus, we analyzed scales from 2^1 through 2^n to 2^9 where n was incremented in units of 0.1. Third, the wavelet scale is not necessarily equivalent to the Fourier period, which is the equivalent scale measure that is of interest. Thus, we transformed the wavelet scale into the equivalent Fourier period, and hence frequency, prior to visualization of results [*Torrence and Compo*, 1998]. Finally, we determined whether or not the particular fit of a wavelet for a given n and s was statistically significant. *Torrence and Compo* [1998] show that the most appropriate method for doing this is based upon choice of an appropriate background spectrum that is associated with noise: if a point (at t, s) in the wavelet power spectrum is statistically distinguishable from the associated point in the background spectrum, then it can be assumed to be a significant fit at the confidence level chosen for the analysis. As is commonly observed in velocity time series, we assumed that white noise would be present [*Biron et al.*, 1998].

4. Results

4.1. Time-Averaged Flow Fields

[16] The time-averaged flow fields for the downstream u and vertical w velocity components (Figure 2) show the influence of the bed topography on the near-bed flow. Analysis of the time-averaged downstream u component for the three different Reynolds numbers (Figures 2a–2c) shows areas of recirculation in the wakes of protruding

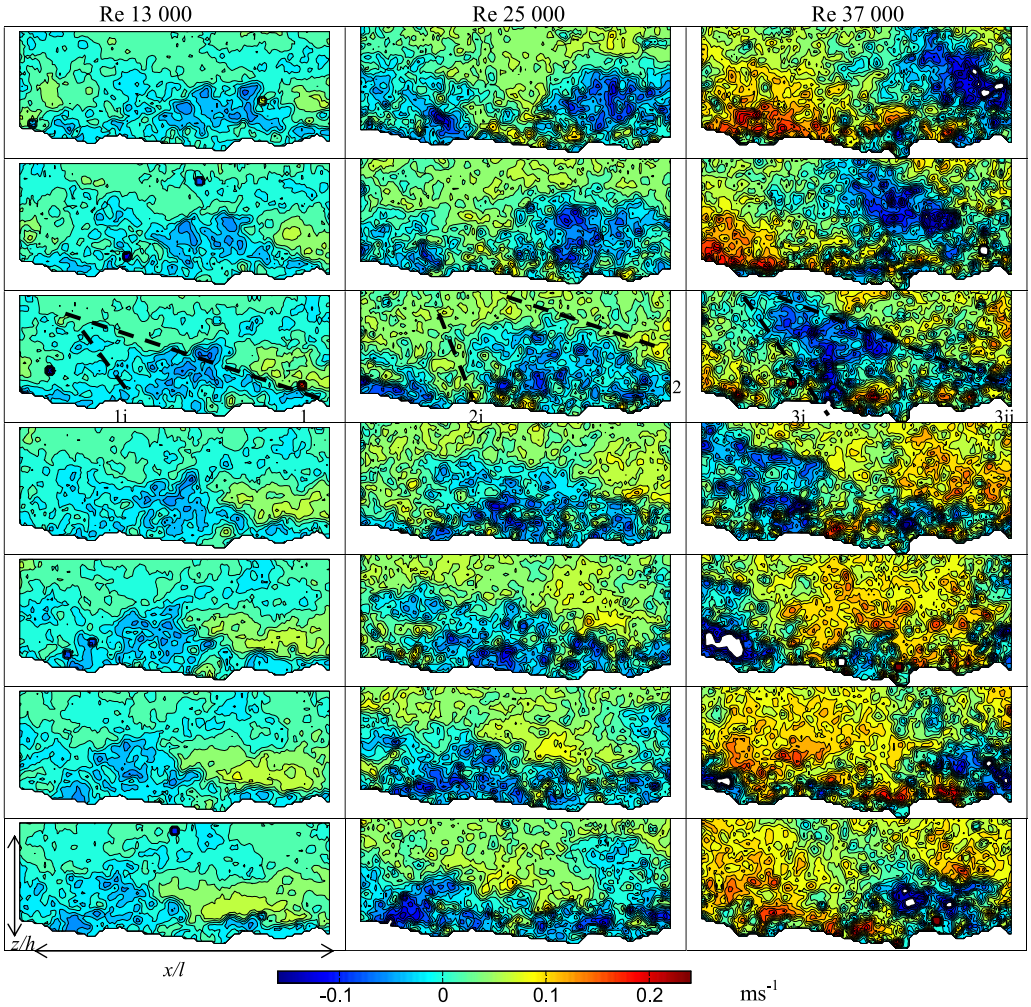

Figure 3. A time series of the instantaneous *u* component of velocity minus 0.85 mean *u* component. Each image is separated by 0.1333 s in increasing time steps down the figure; *z*/*h* is equal to 0.12 m, and *x*/*l* is equal to 0.25 m. For each of the images the flow is from right to left. The dotted lines represent visual detection of the front and the back of the structures.

clasts, above which there in an increase in average flow velocity with depth. The local recirculation identified in the *u* component appears over a short distance (∼0.03 m; region A in Figure 2a). The vertical *w* component more clearly identifies regions of both separation and reattachment of flow over individual particles which are not necessarily defined in the *u* component (region B in Figure 2e). These regions have a downstream length of ∼0.04 m that appears consistent for all Reynolds numbers. In addition, the *w* component identifies a larger region of reattachment, which exists for all three *Re* numbers, that is generated from a larger clast upstream (region C in Figure 2f), and which extends over a downstream distance of ∼0.1 m. Although these images are of the mean values, and individual coherent flow structures are thus not identified, the effect of the topographic protrusion of bed forms is clearly seen to influence the whole flow field.

4.2. Instantaneous Flow Visualization

[17] Analysis of the instantaneous downstream *u* velocity component of flow for the three different Reynolds numbers, through a series of consecutive images, provides a visualization of flow over the gravel surface (Figure 3). Following the recommendation of *Adrian et al.* [2000], the simplest approach to analyze a turbulent flow is to decompose the field into a constant streamwise velocity plus the deviatoric component. There is no dynamical basis for preferring one frame of reference, and the one that provides the best visualization should be used [*Adrian et al.*, 2000]. In the present study, the instantaneous *u* component of velocity minus 0.85 of the mean value is mapped, enabling better detection and visualization of vortical structures within the flow.

[18] All of the images demonstrate the highly variable nature of flow over the gravel surface and turbulent structures close to the bed can be detected visibly: these are clearly seen as "bulges" of lower-velocity fluid originating at the bed and intruding into the outer flow at all three Reynolds numbers. These bulges of fluid are most visibly detectable at *Re* = 37,000, where it can be seen that they extend throughout the entire image (Figure 3) which equates to 0.7 of the flow depth. The back of these large-scale turbulent structures adopt a defined boundary, sloping upstream at an angle visually estimated to be ∼30° (marked as dotted line 3ii in Figure 3). It is more difficult to define

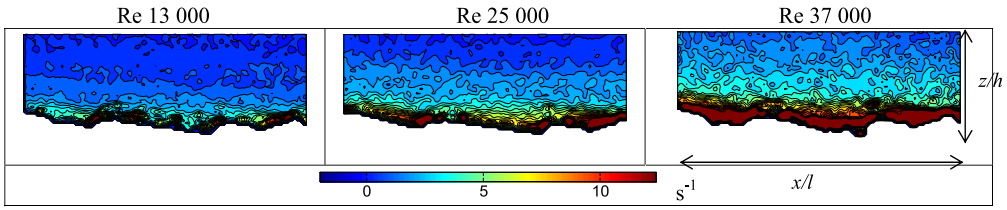

Figure 4. Time-averaged *uw* vorticity (ω)y for three Reynolds numbers: 13,000, 25,000, and 37,000. Flow direction is from right to left; z/h is equal to 0.12 m, and x/l is equal to 0.25 m.

the front of the structure visually, although the downstream lead angle appears to be steeper at ~45° (marked as dotted line 3i in Figure 3) than the rear, upstream back of the structure. There is also an apparent decrease in the streamwise velocity toward the back of the flow structure, with a clearly defined region of higher-velocity flow between each of these low-velocity structures (Figure 3). These features decrease in their distinctiveness at lower Reynolds numbers; the rear, upstream angle of the structures decreases and they are not visible as far from the bed (lines 1 and 2 in Figure 3). However, these features do show similar geometric characteristics to those formed at Re = 37,000, with the lower streamwise velocity flow being located closer to the back of the structure, and the downstream lead angle appearing steeper but harder to define clearly (lines 1i and 2i in Figure 3). Furthermore, the distance between these structures appears to increase at higher Reynolds number. In summary, as the Reynolds number increases, then the visual distinctiveness of these structures becomes more apparent as (1) they become visible through the whole image, which equates to ~0.7 of the flow depth, (2) the downstream slope of the coherent structure increases, (3) the decrease in streamwise flow velocity toward the back of the structure becomes greater, and (4) the spacing between these coherent flow structures increases. These observations agree with previous work which showed that at higher flow velocities the development of coherent flow structures became more pronounced [*Shvidchenko and Pender*, 2001]. Furthermore, our results appear to visualize structures similar to the classical bursting phenomenon in which low-momentum fluid is ejected from the bed [*Grass*, 1971; *Talmon et al.*, 1986; *Shen and Lemmin*, 1999; *Roy et al.*, 2004; *Lacey et al.*, 2007], although here this is clearly seen to be developing over the large anchor clasts in the bed. Studies in the turbulent boundary layer over a flat surface have also suggested a change in the form and angle of hairpin vortices that is dependent on the flow Reynolds number [*Head and Bandyopadhyay*, 1981]. *Head and Bandyopadhyay* [1981] illustrate that at higher Reynolds numbers, the number of hairpins traversing the boundary layer decreases, but the vortices still penetrate through the entire boundary layer, as also revealed in the present study over rough gravel surfaces.

4.3. Time-Averaged and Instantaneous *uw* Vorticity

[19] Analysis of the time-averaged and instantaneous *uw* vorticity enables an improved understanding of the magnitude and spatial distribution of the turbulent stresses in the flow field. The time-averaged flow fields for the *uw* vorticity (Figure 4) show the influence of the bed topography on the near-bed flow for the three different Reynolds numbers. Regions of high vorticity ($\omega > 12$ s^{-1}) are located close to the bed (<0.1 z/h) for all three Reynolds numbers, with vorticity decreasing in intensity away from the bed. For Re = 13,000, areas of high vorticity are found in localized regions around large clasts, but as the Reynolds numbers increases the high-vorticity zones become more continuous and influence more of the flow depth. Topographic protrusions from the bed are clearly seen to generate vorticity, although, as these images are time-averaged, individual coherent flow structures cannot be identified [*Agui and Andreopoulis*, 1992] nor is it possible to determine the typical spatial and temporal persistence of individual flow structures originating from individual clasts.

[20] Analysis of the instantaneous *uw* vorticity of flow for the three different Reynolds numbers, through a series of consecutive images similar to the analysis of instantaneous velocity (Figure 3), provides a visualization of flow over the gravel surface (Figure 5). The flow maps presented are for the equivalent time steps to the instantaneous *u* component flow fields shown in Figure 3. All of the images demonstrate the highly variable nature of flow over the gravel surface and that turbulent structures close to the bed can be detected visibly. Furthermore, as observed in the time-averaged flow fields, as the Reynolds number increases a continuous band of high (>15 s^{-1}) vorticity forms in the near-bed region (<0.1 z/h). However, for all three Reynolds numbers, the vorticity appears to originate from the bed and oscillate between two forms (marked with dotted lines in Figure 5) that possess a shallow and a steeper angle, possibly representing the front and back of the flow structure. As revealed in the detection of flow structures using the *u* component, the angles of the regions of high-intensity vorticity that originate from the bed become steeper as the Reynolds number increases. Finally, as the Reynolds number increases there appear to be more topographic protrusions on the bed that have the potential to generate vortices.

4.4. Turbulence Intensity

[21] Turbulence intensity was evaluated using the RMS value of each velocity component at each point and reveals (Figure 6) regions of highly turbulent flow in the near-bed region. Similar to the results shown for the *u* component of flow, the greatest turbulence intensity in the near-bed region occurs at higher Reynolds numbers, although by 0.5 z/h the turbulence intensity becomes comparable for all three Reynolds numbers for both components of velocity. For Re = 37,000, a band of intense turbulence extends from the bed to approximately 0.2 z/h and is present across the whole of the field of view, except in the lee of the protruding clasts, where skimming flow accelerates fluid across the top of the particle (see Figure 2) and a recirculation zone exists between the clast and downstream reattachment point.

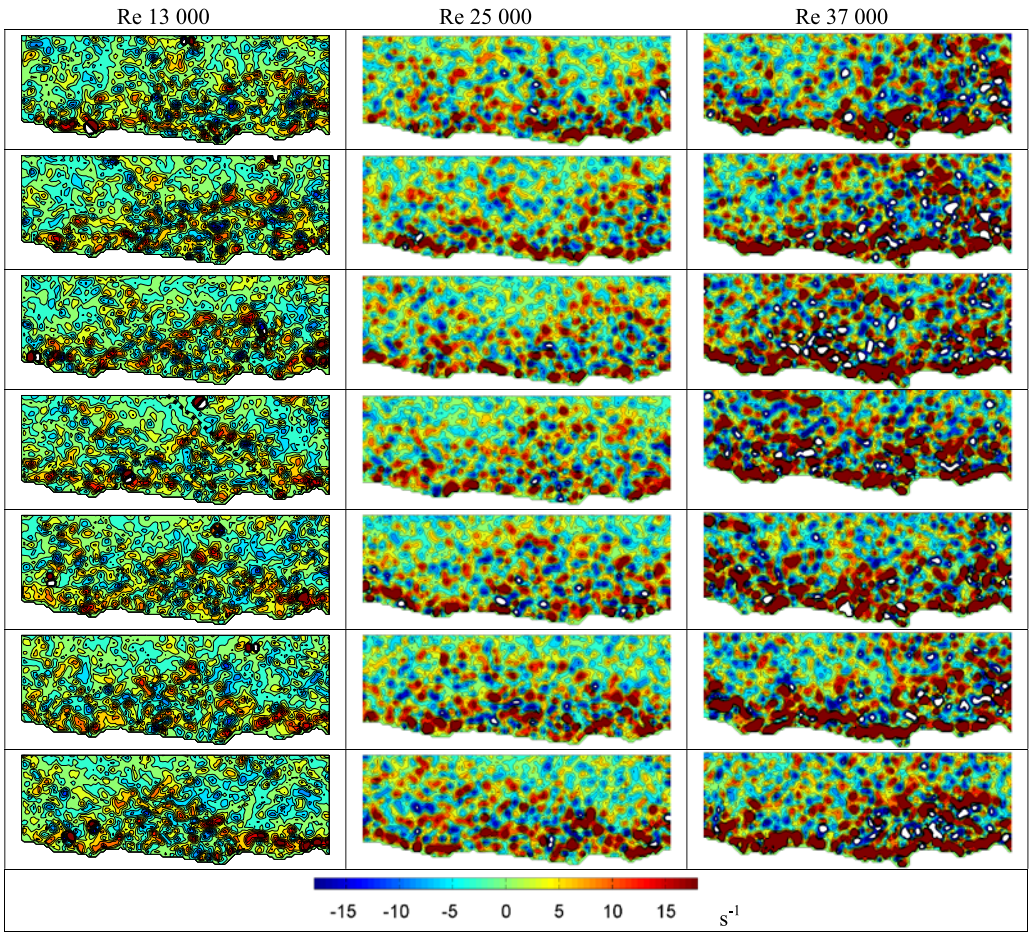

Figure 5. A time series of the instantaneous *uw* vorticity (ω). Each image is separated by 0.1333 s and corresponds to the same time step as the instantaneous *u* velocity component in Figure 3; z/h is equal to 0.12 m, and x/l is equal to 0.25 m. For each of the images the flow is from left to right.

However, there appears to be a threshold spacing at which this occurs, which scales with the relative protrusion of the upstream clast. As the Reynolds number increases, this intense band of turbulence intensity increases in its spatial extent and more localized regions of turbulence generation associated with individual clasts become less distinct. These regions of discrete higher turbulence intensity at lower flow Reynolds numbers appear to be linked to shear layers that form over individual clasts. At low *Re*, these near-bed flow structures are related to the wakes of individual obstacle clasts, and jetting of higher-velocity flow between such clasts, and they may not penetrate vertically within the flow to much above the tops of the obstacles. Therefore, the effect of the bed morphology is more apparent at lower flow Reynolds numbers, with the flow field becoming dominated at higher Reynolds number by a fixed band of intense turbulence that is formed as reattachment lengths increase. At higher-flow Reynolds numbers, it appears that the shear layers associated with flow separation around the larger clasts may ''amalgamate'' and form a more unified region of higher turbulence intensity at $z/h \sim 0.2$.

4.5. Quadrant Analysis

[22] Quadrant 2 and quadrant 4 events are typically given most emphasis in boundary layer studies in order to analyze the extraction of energy from the mean flow field as part of turbulence generation, as they contribute positively to the bed shear stress. However, *Nelson et al.* [1995] demonstrated the importance of quadrant 1 events as being the most effective, although least common, flow structures as regards sediment entrainment. The distribution of all four quadrants over the gravel surface (Figure 7) is consistent with previous observations in that the relative contribution of each quadrant, in terms of both magnitude and spatial distribution, remain similar at all three Reynolds numbers [e.g., *Nelson et al.*, 1995], with quadrant 4 events dominating the distribution in terms of magnitude [*Nelson et al.*, 1995]. However, more localized patterns of flow structures can be identified. In the near-bed region (<0.15 z/h), alternating patterns of quadrant 2 (stoss side) and quadrant 4 (lee side) events are observed, demonstrating localized topographic forcing of the flow. Furthermore, a dominant band of quadrant 2 events is observed higher in the flow (>0.3 z/h). This identifies large-scale vorticity, potentially generated by Kelvin-Helmholtz instabilities that are formed along the leeside shear layers [*Bennett and Best*, 1995; *Best*, 2005], which lie just above the region of maximum RMS values (Figure 4). This vorticity must originate from flow structures generated upstream, outside the field of view, as observed in the *w* component in Figure 2, although the shear layer can be seen to be ''fed'' (lines 1, 2, and 3ii in Figure 3) from

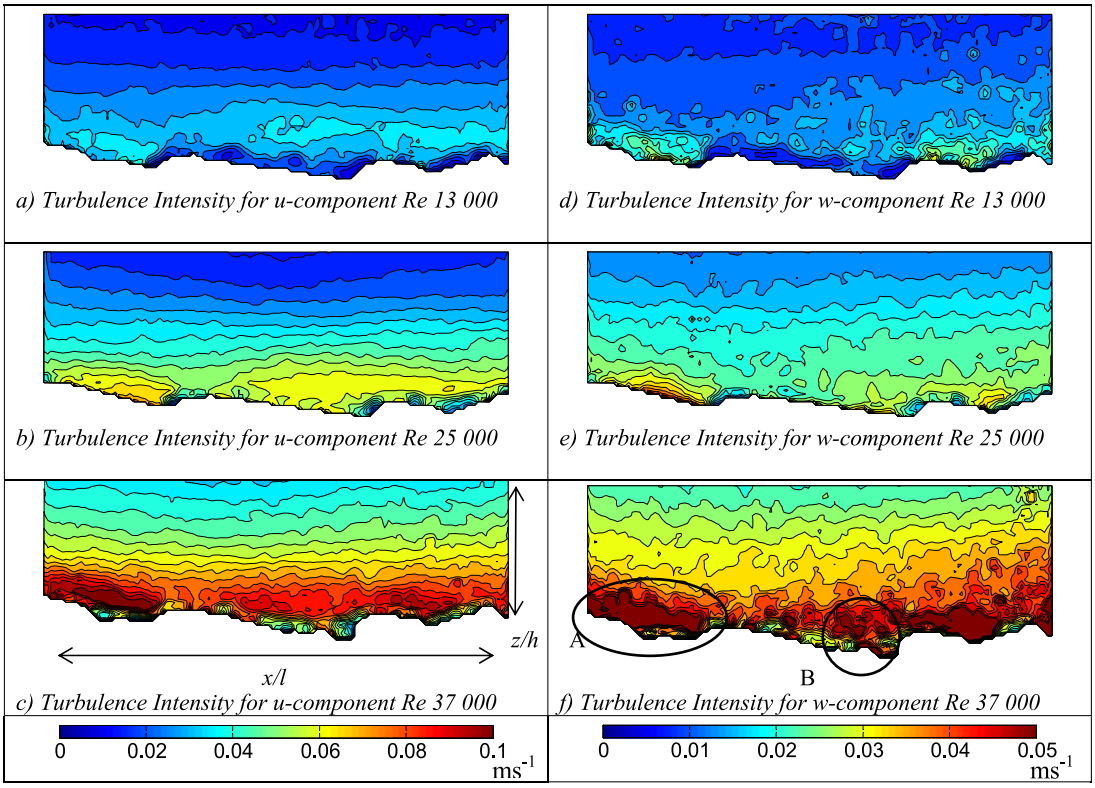

Figure 6. The turbulence intensity calculated as the root-mean-square of the velocity derivative for (a, b, c) *u* component and (d, e, f) *w* component of velocity and three Reynolds numbers: 13,000 (Figures 6a and 6d), 25,000 (Figures 6b and 6e), and 37,000 (Figures 6c and 6f); *z*/*h* is equal to 0.12 m, and *x*/*l* is equal to 0.25 m. A and B represent regions where flow structures originate associated with wake flapping close to the bed.

coherent flow structures originating from the bed. When quadrant 1 and quadrant 3 events are studied, a similar alternating pattern is apparent in the near-bed region as shown in the relationship between quadrants 2 and 4. Quadrant 1 events are located on the stoss side of particles with quadrant 3 events occurring in the lee side. Therefore, as the flow approaches the particle, it decelerates or reverses close to the bed, but otherwise accelerates as it is forced over (or around) the particle. Localized flow deceleration and recirculation occurs in the separation zones that form downstream of the large anchor clasts, and a shear layer is also associated with the horseshoe vortex formed around the stoss side of each clast [*Lawless*, 2004] and that extends downstream.

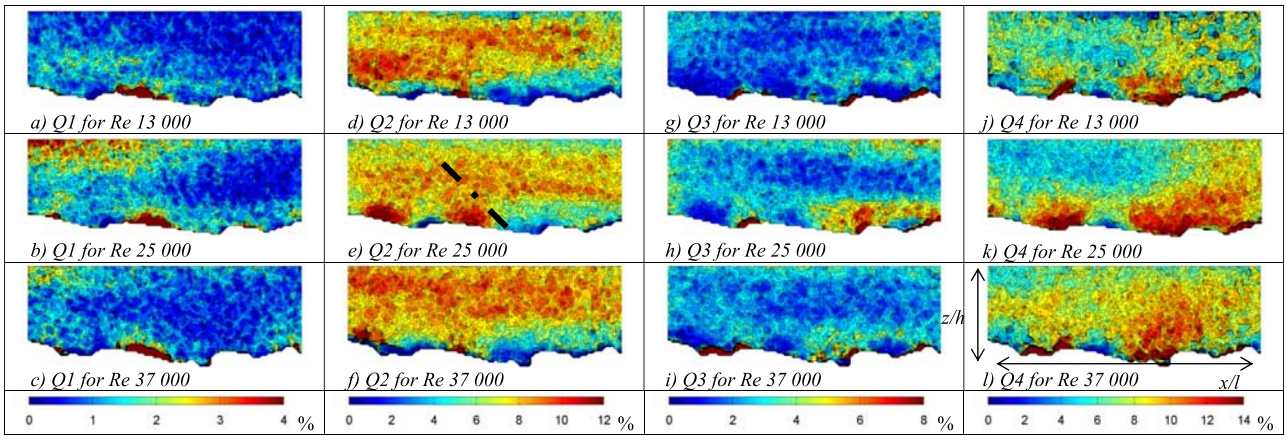

Figure 7. The flow structure as examined through quadrant analysis, (a, b, c) quadrant 1 (Q1), (d, e, f) quadrant 2 (Q2), (g, h, i) quadrant 3 (Q3), and (j, k, l) quadrant 4 (Q4), and three Reynolds numbers, 13,000 (Figures 7a, 7d, 7g, and 7j), 25,000 (Figures 7b, 7e, 7h, and 7k), and 37,000 (Figures 7c, 7f, 7i, and 7l); *z*/*h* is equal to 0.12 m, and *x*/*l* is equal to 0.25 m.

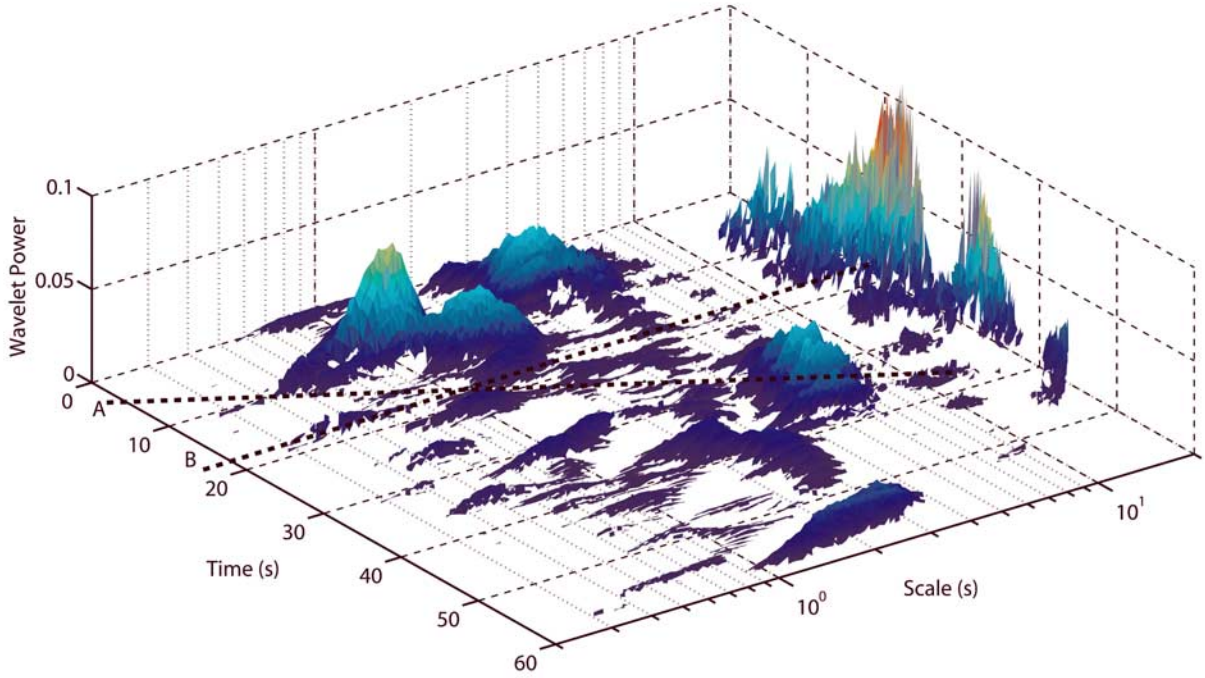

Figure 8. An example of a three-dimensional wavelet power spectrum from Re = 25,000 at 0.4 z/h for the downstream u component of flow. Line A highlights a sequencing of events when either long- or short-period structures can follow each other, while line B demonstrates when they can occur together.

4.6. Wavelet Analysis

[23] The final part of the analysis of flow over this gravel bed examines the velocity time series by application of wavelet analysis, as expressed in four plots (Figures 8–11). This approach is initially demonstrated for one time series (Re = 25,000, x/l = 0.64, z/h = 0.4; see Figure 8), in which the wavelet power spectrum has the length of the time series (60 s) on the abscissa and the temporal length scale (in seconds) of the identified turbulent structures on the ordinate axis. This wavelet power spectrum identifies three distinct periodicities at 1.5, 4, and 10 s (Figure 8), which at a mean velocity of 0.155 m s^{-1} (Table 1) equates to wavelengths of 0.25, 0.62, and 1.55 m (or 0.775, 2.07, and 5.17W, where W is the flume width (= 0.30 m)). The 10-s periodicity is returned to later, but if the periodicities at 1.5 and 4 s are examined (Figure 8), a sequencing of events is apparent where it appears that both short- and long-period structures can either follow each other (line A in Figure 8) or occur together (line B in Figure 8), or may "merge." This implies either potential superimposition or coalescence of flow structures where larger structures may be created by the amalgamation of numerous smaller-scale structures [*Head and Bandyopadhyay*, 1981; *Smith et al.*, 1991] or that there are smaller-scale structures superimposed upon the larger-scale motions.

[24] Here, it is suggested that the periodicity of ~10 s is not a periodicity linked to the near-bed flow at these Reynolds numbers but is more likely to be a product of secondary circulation caused by the width:depth ratio of the flume channel. In straight channels with an aspect ratio of less than 5 (flume width:flow depth, which is 1.5 in this study), turbulence anisotropy at the channel corners generates streamwise secondary circulation that extends into the centre of the channel [*Nezu and Rodi*, 1985]. Such channel width–scale secondary flows have been speculated to have a wavelength of ~6W [*Yalin*, 1992], and the 10-s periodicity, or 5.2W at Re = 13,000, appears to match this scaling. Although secondary flow is typically only a few percent of the average flow velocity, it may have an important effect on the flow structure [*Colombini*, 1993]. In order to remove this periodicity from the time series, the dyadic number is reduced to 2^6 to give a maximum identifiable frequency of 5.25 s. The wavelet power spectrum was then recalculated at heights of 0.2, 0.4, 0.6, and 0.8 z/h for the three different experimental conditions. This further demonstrates the advantage of wavelet analysis in the breakdown and understanding of a time series (Figure 9).

[25] Analysis of several time series at different heights above the bed (Figure 9) shows the same general trends as identified in Figure 8, but with some subtle differences dependent on either location above the bed or flow Reynolds number. Three general features are apparent: (1) several different temporal scales of structure (0.5, 1, 1.5, 2, and 4 s) are present, (2) there is an apparent sequencing of events, with longer-period structures following shorter-period events, and (3) flow structures of different temporal resolution may pass through the same point at the same time. However, there appears to be greater structure and organization in the lower-frequency turbulence signal at lower Reynolds numbers. For example, if Figure 9r is compared to Figure 9b, the structures with temporal periodicities of ~4 s appear to persist throughout the 60 s at Re = 13,000, whereas these events are more intermittent at Re = 37,000. This trend is consistent throughout the flow

Figure 9. The wavelet power spectra for both (a, b, c, d, i, j, k, l, q, r, s, t) the *u* velocity component and (e, f, g, h, m, n, o, p, u, v, w, x) the *w* velocity component for three Reynolds numbers: 37,000 (Figures 9a–9h), 25,000 (Figures 9i–9p), and 13,000 (Figures 9q–9x). The wavelet power spectra have the length of the time series (60 s) on the abscissa and the temporal length scale (in seconds) of the identified turbulent structures on the ordinate axes. The lines on Figure 9c identify an increase in temporal length scale of structures passing through the point.

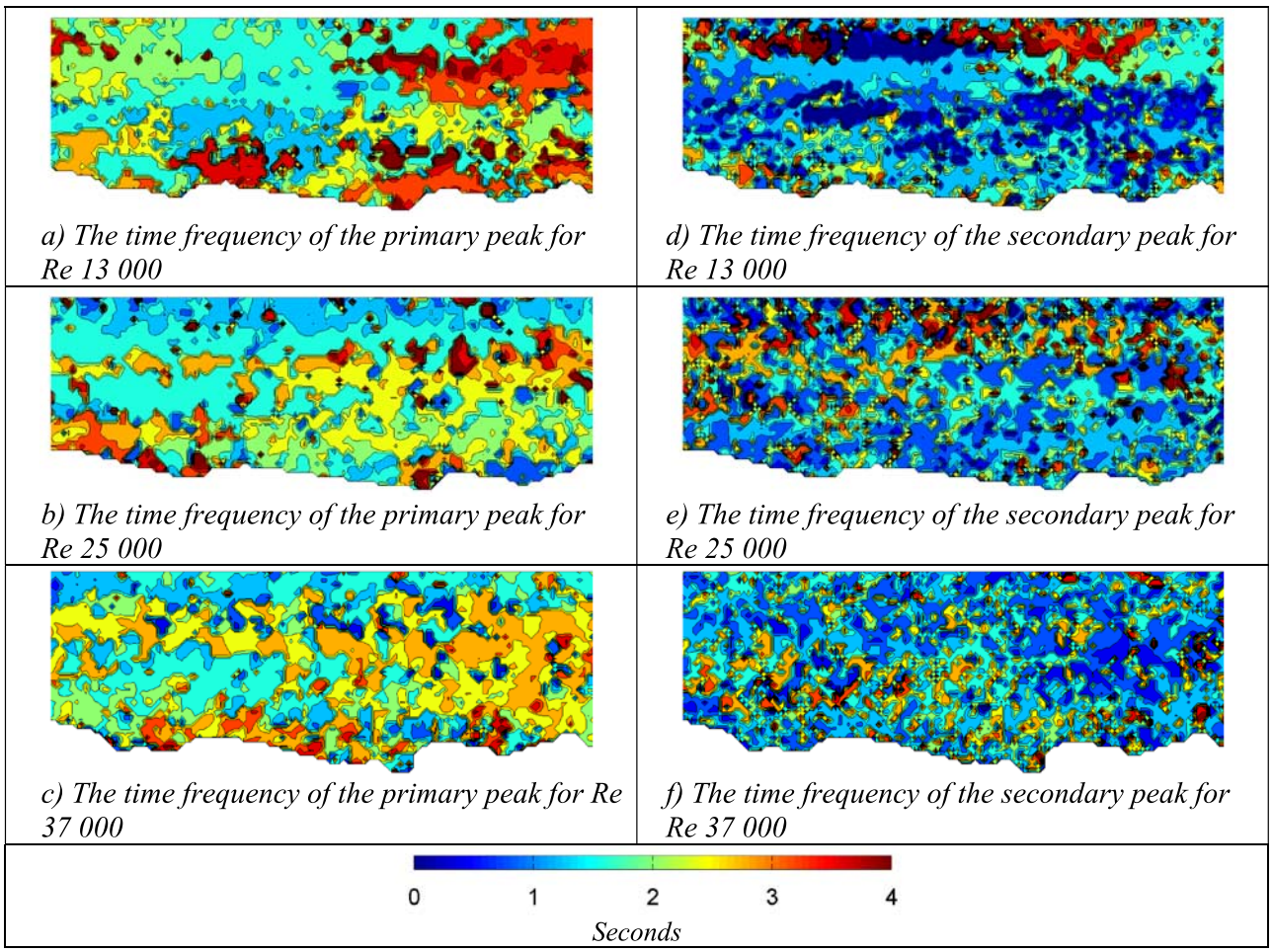

Figure 10. The time frequency of (a, b, c) the primary peaks and (d, e, f) the secondary peaks calculated in the time-averaged wavelet power spectrum for three Reynolds numbers: 37,000 (Figures 10c and 10f), 25,000 (Figures 10b and 10e), and 13,000 (Figures 10a and 10d).

depth. For Re = 37,000, the frequencies <1 s are dominant, especially at 0.2 z/h, while their detection is minimal for Re = 13,000. This suggests that the higher-frequency scales become more important, and the lower frequency less important, as the Reynolds number increases.

[26] For Re = 37,000, there visually appears to be more sequencing of flow structures, especially at heights of 0.4 to 0.8 z/h, with frequencies from 1 to 3 s. On Figure 9c, two consecutive dotted diagonal lines illustrate an increase in the temporal length scales of structures passing through the point, implying that larger temporal scale structures are forming at a location downstream. Finally, as the Reynolds number increases, especially at Re = 37,000, the 5-s periodicity ceases to exist.

[27] Although yielding a unique insight into the temporal dynamics of coherent flow structures over this gravel bed, this form of Eulerian analysis does not enable the detection of changes in the entire flow field as Reynolds number increases. Primarily, it is difficult to detect major changes through the profile (from 0.2 to 0.8 z/h) as these flow structures appear to influence the whole flow depth. Second, it is difficult to distinguish any major differences between the u and w components, and the flow structures appear to be two-dimensional. Consequently, the analysis was expanded to study the entire flow field by calculation of the time-averaged wavelet power spectrum for every point in the field of view, which permitted identification of the two main peaks in the spectrum and their associated temporal frequency (Figure 10). The most obvious difference between the primary and secondary peaks is that much larger, spatially coherent regions of similarity are observed in the primary peak. This includes a region with similar temporal length scales at a height of ~0.4 z/h. These flow structures at this height have a time scale of ~3 s for Re = 37,000, and the structures decrease in both their period and the height to which they influence the flow field as the Reynolds number decreases (2.5 s for Re = 25,000 and 1.5 s for Re = 13,000). Moreover, these bands appear clearly linked to the bed (Figure 10) implying that the turbulent flow structures are generated in the near-bed region and then advected into the flow above. This is in agreement with previous work where an outer zone has been defined where oscillatory structure growth and breakups predominate [*Kim et al.*, 1971] and has been classified as the wake layer [*Nowell and Church*, 1979]. Furthermore, some longer periodicities (>4 s) occur close to the bed, and are most detectable for Re = 13,000, although these structures do not appear to move up into the main flow depth. For the secondary peak, these clearly

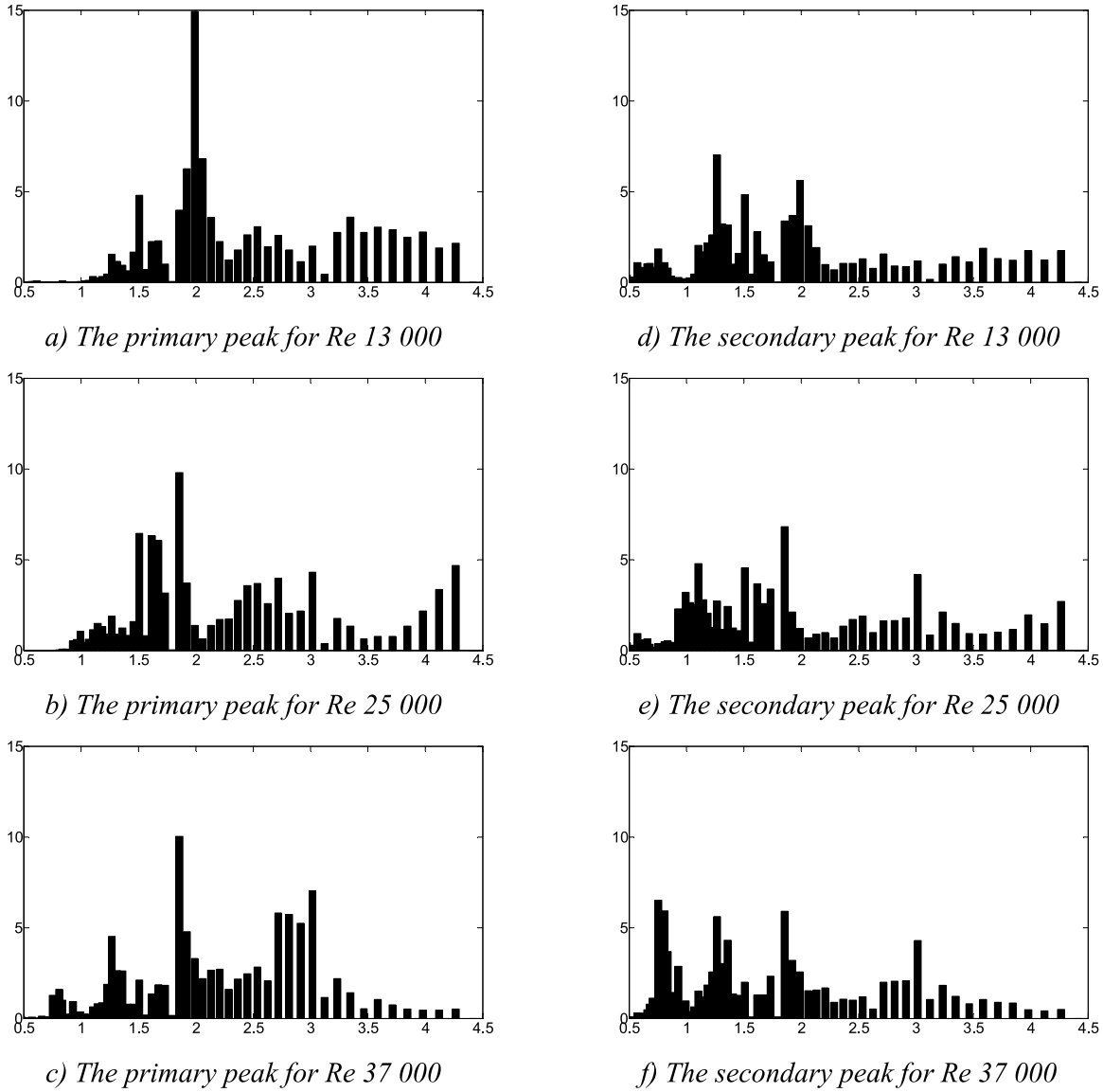

Figure 11. The distribution of the time peaks for (a, b, c) the primary peaks and (d, e, f) the secondary peaks identified in the time-averaged wavelet power spectrum for three Reynolds numbers: 37,000 (Figures 11c and 11f), 25,000 (Figures 11b and 11e), and 13,000 (Figures 11a and 11d). On the abscissa axis is the temporal length scale (in seconds) of the identified turbulent structures, and on the ordinate axis is the percentage of the total number of structures identified.

defined regions are not as visible as the primary peak, especially for Re = 25,000 and Re = 37,000 (Figure 8). However, a similar band to that observed in the primary peak is identified for Re = 13,000 at a similar height above the bed (z/h = 0.3), with a periodicity of 1.25 s. The geometric similarity with the primary peak for Re = 37,000 may suggest it is the same physical processes which generates these flow structures, although the influence of this period on the flow field decreases at lower Reynolds numbers, where it is absent at Re = 13,000. The same "streaky" patterns of structures, originating from the bed and moving up into the flow, are observed, with the temporal scale of these structures depending greatly on the local bed structure.

[28] In order to collapse the data displayed in Figure 10, the time frequencies have been grouped into wavelet frequency time bins (a nonlinear scale) in Figure 11. Collapsing the signal using this approach enables detection of the frequency of the formative mechanisms generating these coherent flow structures, with the results being presented as a percentage, for each time bin, of the total number of structures detected. For the primary peak, it is clear that the dominant periodicity is $\sim$2 s and is present at all three Reynolds numbers, although its contribution to the total number of structures decreases from 15% at Re = 13,000 to 10% at Re = 37,000. Furthermore, as the Reynolds number increases to Re = 37,000, higher-frequency structures

Table 3. Estimation of Reattachment Lengths From Frequencies Identified in Collapsing the Entire Flow Field Flow Frequencies[a]

	Frequency (Hz)			
	1.33	0.80	0.50	0.33
	Vortex Shedding $f_v = 0.6U/X_r$			
Re = 13,000	~0.07	~0.12	~0.19	~0.31
Re = 25,000	~0.13	~0.26	~0.36	~0.54
Re = 37,000	~0.19	~0.32	~0.52	~0.79
	Wake Flapping $f_w < 0.1U/X_r$			
Re = 13,000	~0.011	~0.014	~0.031	~0.047
Re = 25,000	~0.023	~0.038	~0.06	~0.091
Re = 37,000	~0.033	~0.054	~0.087	~0.132

[a]Reattachment lengths are measured in meters.

become more apparent at ~1.25 and ~0.75 s. However, the most dominant change as Reynolds number increases is the appearance of a period at ~3 s that makes the distribution bimodal. More subtle trends can be observed in the secondary peak data in Figures 9d–9f, similar to that revealed in the analysis of secondary peaks shown in Figure 10. Structures with a frequency of ~2 s are detected for all three Reynolds numbers (Figures 11d–11f) with shorter-frequency structures, again at ~1.25 s, also being present. The apparent contribution of the ~1.25-s structures in the secondary peaks appears to decrease as the Reynolds number increases, again with the appearance of a ~0.75-s frequency at Re = 37,000. Thus, although the magnitude of the contribution from these structures changes with Reynolds number, the ~2-s periodicity is detected at all Reynolds numbers, and suggests that the same formative mechanism is generating the coherent flow structures. Furthermore, it appears that as the Reynolds number exceeds a critical threshold, additional processes influence the generation of the flow field and these periodicities are examined below through the application of existing scaling laws.

[29] Several different generalized relationships have been proposed to calculate dimensionless numbers that define the period of large-scale turbulence and aid understanding of the overall turbulence signature, such as the boil periodicity suggested by *Jackson* [1976], the Strouhal relationship [*Levi*, 1983, 1991] or vortex and wake flapping frequencies proposed by *Simpson* [1989]. The underlying problem with all of these relationships is that the flow reattachment point is extremely difficult to determine [*Nelson and Smith*, 1989; *Kostaschuk*, 2000; *Best and Kostaschuk*, 2002], and this is made even more problematic over a gravel bed because of vortices merging into a continuous shear layer. However, *Simpson* [1989] proposed two scaling relations: for vortex shedding

$$f_v = 0.6U/X_r, \quad (1)$$

where f_v is vortex frequency, U is the mean velocity, and X_r is the mean length of the separation zone, and for wake flapping

$$f_w < 0.1U/X_r. \quad (2)$$

Figure 11 provides an approximation of the frequency(s) for the identifiable peaks (0.75, 1.5, 2, and 3 s, which equates to 1.3, 0.8, 0.5, and 0.3 Hz). Furthermore, analysis of the DEM (Figure 1) shows that the maximum particle length in the gravel matrix is 0.14 m and the maximum height is 0.062 m. If equations (1) and (2) are rearranged to calculate the reattachment length by using the hydraulic conditions given in Table 2, a second-order approximation of processes generating the turbulent flow field can be deduced (Table 3).

[30] By applying the scaling laws to the four identified frequencies and three hydraulic conditions, the calculated mean lengths of flow separation from wake flapping are between 0.01 and 0.13 m. It is suggested that these are

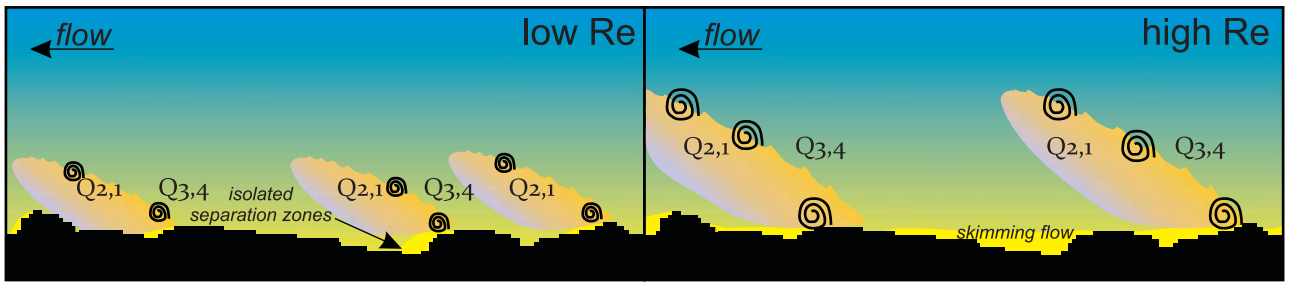

Figure 12. A schematic model of flow over a gravel bed at two Reynolds numbers. At low *Re*, isolated separation zones develop in the leeside of large anchor clasts, and both eddy shedding and wake flapping produce a region of higher turbulence at ~0.4 *z*/*h* (at the level of quadrant labels (Q1–Q4)). At higher *Re*, a region of near-bed skimming flow is created because of interacting separation zones, and larger coherent flow structures are generated that extend farther above the bed, are steeper in the upstream angle, and have a longer period. These flow structures produce a region of higher turbulence at ~0.5–0.6 *z*/*h* (at level of quadrant labels (Q1–Q4)). At each *Re*, note the superimposition and amalgamation of different temporal and spatial scales of flow structure and the origin of the large-scale turbulence associated with the major bed roughness. Colors denote approximate streamwise velocities, with low-velocity flow associated with flow near the bed, and the large-scale flow structures showing low-velocity regions toward the back (upstream) side of the flow structure. The size of the coils reflects the intensity of the structure.

reasonable length scales for flows over such complex heterogeneous topography with a median particle height of 0.02 m and maximum particle length of 0.14 m. Because of the several (temporal) scales of turbulence that have been identified (Figures 10 and 11) and the apparent amalgamation of flow structures into an intense band of turbulence (Figure 6), it may not be possible to separate individual processes of coherent flow structure generation. This is due to the complex bed topography, where each topographic protrusion generates its own flow field and the considerable positive feedback between bed form topography and the generation of flow structures.

[31] However, as demonstrated in Figure 11, the 2-s structure is prevalent for all three Reynolds numbers. The mean lengths of flow separation calculated for wake flapping range from 0.03 to 0.09 m as the Reynolds number increases. Furthermore, when the w component of mean flow (Figure 2) and turbulence intensity (Figure 6) are studied, flow structures with length scales of the same order of magnitude are identified. As discussed previously, flow structures with a length scale of $\sim$0.04 m are clearly detected in the time-averaged images. These flow structures are intermittent and therefore the whole structure will not necessarily be detectable in a time-averaged analysis, since the patterns of structure motion would not be regular. However, the point from where these structures are initiated and generated will be consistent. The same observations can be made in the plots of turbulence intensity (regions A and B in Figure 6) where regions of $\sim$0.07 m length with high turbulence intensity are detected behind protruding clasts. Thus, these structures may be associated with wake flapping close to the bed and its interaction with the protruding topography. This follows classical hydraulic theory that would suggest that as flow approaches an obstacle, a localized area of low flow velocity develops in front of the topographic protrusion and a suppressed saddle point vortex forms [*Hunt et al.*, 1978]. This flow thus moves around such topographic protrusions in the form of tertiary vortices [*Hunt et al.*, 1978] and it is reasoned that these, together with wake flapping associated with the leeside flow separation zone shear layer, may form the coherent flow structures documented herein. This mechanism is possible for all four identified frequencies, with wake flapping reattachment lengths ranging from 0.01 to 0.13 m. Finally, at Re = 37,000, shorter periodicities are identified, which provides an average vortex shedding reattachment length of 0.19 m, similar to that identified at this Reynolds number in Figure 2.

5. Discussion

[32] This analysis has examined the characteristics of turbulent flow generated over known gravel bed topography at three different flow Reynolds numbers. The analysis has detected coherent flow structures with defined spatial and temporal characteristics that scale with the flow Reynolds number. As the Reynolds number increases (Figure 12) (1) the visual distinctiveness of the flow structures becomes more defined through the flow depth, (2) the upstream slope of the coherent flow structure increases in angle, (3) the reduction in streamwise flow velocity, and turbulence intensity, toward the upstream side of the structure increases, and (4) the spacing between these coherent flow structures increases. The source of these structures is identified through examination of the mean and turbulent intensity values, as well as by quadrant analysis. Analysis of the mean u and w components identifies flow recirculation over short distances ($\sim$0.03 m) that is generated by flow separation associated with individual clasts. In addition, a secondary ''reattachment structure'' is identified in the w component with a length scale of $\sim$0.1 m. This localized separation and reattachment is further identified in the turbulence intensity plots where the greatest turbulence intensity is detected in the near-bed region. At higher Reynolds numbers, a continuous band of high turbulence intensity is formed that appears linked to the amalgamation of shear layers associated with flow separation around the larger clasts, thus forming a more unified region of higher turbulence intensity at $\sim$0.2 z/h. By 0.5 z/h, the turbulence intensity becomes comparable for all three Reynolds numbers. Finally, in the near-bed region, quadrant analysis identifies alternating patterns of quadrant 2 (stoss side) and quadrant 4 (lee side) events, again demonstrating localized bed/topographic forcing of the flow. Furthermore, a band of quadrant 2 events are detected higher in the flow, most likely formed by large-scale Kelvin-Helmholtz instabilities along a shear layer [e.g., *Bennett and Best*, 1995; *Best*, 2005]. A similar pattern is observed in quadrant 1 (stoss side) and quadrant 3 (lee side) events in the near-bed region, which suggests that as the flow approaches the particle, it decelerates or reverses close to the bed, but otherwise accelerates as it is forced over (or around) the particle. Localized flow deceleration occurs in the separation zones that form downstream of the large anchor clasts: flow within these separation zones recirculates, forming a body-fitted vortex, and a shear layer that extends downstream is associated with each of the clast lee sides.

[33] Wavelet analysis has enabled the temporal length scales of the turbulent signatures to be identified. Decomposing the selected time series in the temporal domain identified general trends which included (1) several different dominant temporal scales of flow structure (0.5, 1, 1.5, 2, and 4 s), (2) an apparent sequencing of events, with longer-period structures following shorter-period events, and (3) flow structures of different temporal resolution passing through the same point at the same time. When the signal is decomposed and analyzed, for the whole image, by detecting the primary and secondary peaks in the wavelet power spectrum, the time scales of the dominant flow structures can be identified. The most obvious difference between the primary and secondary peaks is that much larger, spatially coherent regions of similarity are observed in the primary peak, and includes a region with similar temporal length scales at a height of $\sim$0.4 z/h. The flow structures at this height have a time scale of $\sim$3 s for Re = 37,000 but, as the Reynolds number decreases, are seen to decrease in both their temporal scale (2.5 s for Re = 25,000 and 1.5 s for Re = 13,000) and the height above the bed at which they influence the flow field. These bands appear linked to the bed (lines A and B in Figure 8), suggesting that turbulent flow structures are generated in the near-bed region and then entrained into the flow above. If this

analysis is extended, the distribution of turbulent length scales identifies a 2-s flow structure that is prevalent at all three Reynolds numbers. By applying standard scaling laws, the mean lengths of flow separation calculated for wake flapping range from 0.03 to 0.09 m and increase at higher Reynolds numbers.

[34] The results obtained in this analysis agree with previous work in which the development of the flow structure has been found to be proportional to the flow velocity (i.e., Reynolds number if flow depth is kept constant [*Shvidchenko and Pender*, 2001]), and identifies structures similar to the classical bursting phenomenon in which low-momentum fluid is ejected from the bed [*Grass*, 1971; *Talmon et al.*, 1986; *Shen and Lemmin*, 1999]. However, the present study shows that these flow structures develop over the large anchor clasts in the bed, potentially by wake flapping. Studies of turbulent boundary layers over flat surfaces have also suggested a change in the form and angle of hairpin vortices dependent on the flow Reynolds number [*Head and Bandyopadhyay*, 1981], with the hairpin vortices becoming stretched and narrower at higher *Re.* At higher Reynolds numbers, the number of hairpins traversing the boundary layer was found to decrease, although the vortices still penetrated through the entire boundary layer, and can merge to form ''packets'' of hairpin vortices [e.g., *Christensen and Adrian*, 2001]. Over rough surfaces, these flow structures appear to merge into a single layer, which implies that skimming flow [*Grass*, 1971; *Grass et al.*, 1991; *Krogstad et al.*, 1992] generated over the largest roughness elements tends to dominate as the Reynolds number increases, and may form large-scale vorticity. The present study illustrates that the origin of these larger-scale motions are Kelvin-Helmholtz instabilities generated along the separation zone shear layer [e.g., *Müller and Gyr*, 1982, 1986; *Rood and Hickin*, 1989; *Bennett and Best*, 1995; *Best*, 2005], thus forming a region defined as where oscillatory structure growth and breakups predominate [*Kim et al.*, 1971] and which has previously been classified as the wake layer (wake flapping) [*Nowell and Church*, 1979]. This implies the creation of larger-scale flow structures by either potential superimposition, or coalescence, of numerous smaller-scale structures [*Head and Bandyopadhyay*, 1981; *Smith et al.*, 1991], or where smaller-scale structures exist upon larger-scale structures. Thus, our present analysis suggests that coherent flow structures over gravels owe their origin to bed-generated turbulence and that large-scale outer layer structures are the result of flow-topography interactions in the near-bed region associated with wake flapping.

6. Conclusions

[35] Turbulent flows moving over a gravel bed develop large-scale, macroturbulent flow structures that are initiated at the bed, and grow and dissipate as they move upward through the flow depth. These large-scale flow structures change their form and magnitude at higher Reynolds numbers, becoming more distinct, with a clearer velocity signature and steeper upstream-dipping slopes. This study shows that the near-bed flow controls the flow structure fed into the outer flow and that macroturbulence over gravel beds is sourced from these flow-bed interactions. These large-scale coherent flow structures are separated by regions of higher than average streamwise velocity, and define regions that are dominated by quadrant 2 and quadrant 1 events, which are interspersed with regions dominated by quadrant 4 and quadrant 3 events. At low Reynolds numbers, flow over the gravel surface is found to possess distinct regions of flow separation in the leeside of individual clasts, but as Reynolds number increases and the length of the flow recirculation zones grows, then these amalgamate to form a layer of skimming flow near the bed. Turbulence associated with both eddy shedding and wake flapping in the leeside of these clasts creates the larger-scale coherent turbulent motions, which may amalgamate to form a region of higher turbulence intensity at a dimensionless height away from the bed, z/h, of $\sim$0.5 at higher Reynolds numbers. Superimposition of such motions appears to create the conditions necessary for the formation of large-scale coherent flow structures that can advect through the entire flow depth. Wavelet analysis has been shown to be a powerful tool in deciphering the complex signatures of such large-scale motions, and shows that these organized motions have longer periods at higher Reynolds numbers and penetrate further into the outer flow. The occurrence of several temporal scales of structure, and their presence at the same time, suggest the superimposition and amalgamation of smaller-scale flow structures to create this large-scale turbulence.

[36] Future work clearly needs to investigate further the exact nature of such superimposition, amalgamation and vortex evolution, and investigate the links between the growth and dissipation of these structures, and both sediment suspension and bed load transport. The interactions between such flow structures and sediment entrainment holds the key for understanding and predicting the transport and fate of a range of different size and composition particles both above, at, and within the bed of gravel substrates.

[37] **Acknowledgments.** The authors are grateful to Mark Franklin for assistance with the flume experiments and operation of the DPIV and to J. H. Chandler, University of Loughborough, for the loan of the Kodak DCS 460 digital camera and discussion regarding errors in camera geometry. R.J.H. was funded through NERC fellowship NER/J/S/2002/00663 while the DANTEC DPIV system was funded by NERC JREI grant GR3/JE140 to J.L.B. We are grateful to the Associate Editor and two anonymous referees for providing helpful comments that have led to significant improvements in this manuscript.

References

Adrian, R. J., C. D. Meinhart, and C. D. Tomkins (2000), Vortex organization in the outer region of the turbulent boundary layer, *J. Fluid Mech.*, *422*, 1–54, doi:10.1017/S0022112000001580.

Agui, J. H., and J. Andreopoulis (1992), Experimental investigation of a three-dimensional boundary layer flow in the vicinity of an upright wall mounted cylinder, *J. Fluids Eng.*, *114*, 566–576, doi:10.1115/1.2910069.

Bennett, S. J., and J. L. Best (1995), Mean flow and turbulence structure over fixed, two-dimensional dunes: Implications for sediment transport and dune stability, *Sedimentology*, *42*, 491–513, doi:10.1111/j.1365-3091.1995.tb00386.x.

Best, J. L. (1996), The fluid dynamics of small-scale alluvial bedforms, in *Advances in Fluvial Dynamics and Stratigraphy*, edited by P. A. Carling and M. Dawson, pp. 67–125, John Wiley, New York.

Best, J. L. (2005), The fluid dynamics of river dunes: A review and some future research directions, *J. Geophys. Res.*, *110*, F04S02, doi:10.1029/2004JF000218.

Best, J. L., and R. A. Kostaschuk (2002), An experimental study of turbulent flow over a low-angle dune, *J. Geophys. Res.*, *107*(C9), 3135, doi:10.1029/2000JC000294.

Best, J. L., T. Buffin-Bélanger, A. Kirkbride, and I. Reid (2001), Visualisation of coherent flow structures associated with particle clusters: Temporal and spatial characterisation revealed using ultrasonic Doppler velocity profiling, paper presented at Gravel-Bed Rivers 2000, N. Z. Hydrol. Soc., Christchurch, New Zealand.

Biggs, B., M. Duncan, S. Francoeur, and W. Meyer (1997), Physical characteristics of microform bed cluster refugia in 12 headwater streams, New Zealand, *N. Z. J. Mar. Freshwater Res.*, *31*, 413–422.

Biron, P. M., S. N. Lane, A. G. Roy, K. F. Bradbrook, and K. S. Richards (1998), Sensitivity of bed shear stress estimated from vertical velocity profiles: The problem of sampling resolution, *Earth Surf. Processes Landforms*, *23*, 133–139, doi:10.1002/(SICI)1096-9837(199802)23:2<133::AID-ESP824>3.0.CO;2-N.

Bogard, D. G., and W. G. Tiederman (1986), Burst detection with single-point velocity measurement, *J. Fluid Mech.*, *162*, 389–413, doi:10.1017/S0022112086002094.

Brayshaw, A. C., L. E. Frostick, and I. Reid (1983), The hydrodynamics of particle clusters and sediment entrainment in coarse alluvial channels, *Sedimentology*, *30*, 137–143, doi:10.1111/j.1365-3091.1983.tb00656.x.

Buffin-Bélanger, T., and A. G. Roy (1998), Effects of a pebble cluster on the turbulent structure of a depth-limited flow in a gravel-bed river, *Geomorphology*, *25*, 249–267, doi:10.1016/S0169-555X(98)00062-2.

Buffin-Bélanger, T., and A. G. Roy (2005), 1 min in the life of a river: Selecting the optimal record length for the measurement of turbulence in fluvial boundary layers, *Geomorphology*, *68*, 77–94, doi:10.1016/j.geomorph.2004.09.032.

Butler, J. B., S. N. Lane, and J. H. Chandler (1998), Assessment of DEM quality for characterizing surface roughness using close range digital photogrammetry, *Photogramm. Rec.*, *16*(92), 271–291.

Butler, J. B., S. N. Lane, J. H. Chandler, and K. Porfiri (2002), Through-water close-range digital photogrammetry in flume and field environments, *Photogramm. Rec.*, *17*, 419–439, doi:10.1111/0031-868X.00196.

Carbonneau, P. E., S. N. Lane, and N. E. Bergeron (2003), Cost-effective non-metric close-range digital photogrammetry and its application to a study of coarse gravel river beds, *Int. J. Remote Sens.*, *24*, 2837–2854, doi:10.1080/01431160110108364.

Cellino, M., and W. H. Graf (1999), Sediment-laden flow in open-channels under noncapacity and capacity conditions, *J. Hydraul. Eng.*, *125*, 455–462, doi:10.1061/(ASCE)0733-9429(1999)125:5(455).

Christensen, K. T., and R. J. Adrian (2001), Statistical evidence of hairpin vortex packets in wall turbulence, *J. Fluid Mech.*, *431*, 433–443, doi:10.1017/S0022112001003512.

Clifford, N. J., and J. R. French (1993), Monitoring and analysis of turbulence in geophysical boundaries: Some analytical and conceptual issues, in *Turbulence: Perspectives on Flow and Sediment Transport*, edited by N. J. Clifford, J. R. French, and J. Hardisty, pp. 93–120, John Wiley, New York.

Clifford, N. J., A. Robert, and K. S. Richards (1992), Estimation of flow resistance in gravel-bedded rivers: A physical explanation of the multiplier of roughness length, *Earth Surf. Processes Landforms*, *17*, 111–126, doi:10.1002/esp.3290170202.

Colombini, M. (1993), Turbulence driven secondary flows and the formation of sand ridges, *J. Fluid Mech.*, *254*, 701–719, doi:10.1017/S0022112093002319.

DANTEC Dynamics (2000), FlowMap: Particle image velocimetry instrumentation, *Publ. 9040U3625*, Skovlunde, Denmark.

Dinehart, R. L. (1992), Evolution of coarse gravel bed forms: Field measurements at flood stage, *Water Resour. Res.*, *28*, 2667–2689, doi:10.1029/92WR01357.

Farge, M. (1992), Wavelet transforms and their application to turbulence, *Annu. Rev. Fluid Mech.*, *24*, 395–457, doi:10.1146/annurev.fl.24.010192.002143.

Fidman, B. A. (1953), Principal results of experimental study of the structure of turbulent flows, in *Problem of Channel Processes* (in Russian), edited by N. E. Kondrat'ev and N. N. Fedorov, pp. 138–150, Gidrometeoizdat, Leningrad, Russia.

Fidman, B. A. (1991), *Turbulence in Water Flows* (in Russian), Gidrometeoizdat, Leningrad, Russia.

Grass, A. J. (1971), Structural features of turbulent flow over smooth and rough boundaries, *J. Fluid Mech.*, *50*, 233–255, doi:10.1017/S0022112071002556.

Grass, A. J., and M. Mansour-Tehrani (1996), Generalized scaling of coherent bursting structures in the near-wall region of turbulent flow over smooth and rough boundaries, in *Coherent Flow Structures in Open Channels*, edited by P. J. Ashworth et al., pp. 41–62, John Wiley, New York.

Grass, A. J., R. J. Stuart, and M. Mansour-Tehrani (1991), Vortical structures and coherent motion in turbulent flow over smooth and rough boundaries, *Philos. Trans. R. Soc., Ser. A*, *336*, 35–65, doi:10.1098/rsta.1991.0065.

Grinvald, D. I. (1974), *Turbulence of Open-Channel Flows* (in Russian), Gidrometeoizdat, Leningrad, Russia.

Grinvald, D. I., and V. I. Nikora (1988), *River Turbulence* (in Russian), Gidrometeoizdat, Leningrad, Russia.

Grishanin, K. V. (1990), *Fundamentals of the Dynamics of Alluvial Flows* (in Russian), Transport, Moscow.

Hardy, R. J., S. N. Lane, M. R. Lawless, J. L. Best, L. Elliott, and D. B. Ingham (2005), Development and testing of a numerical code for treatment of complex river channel topography in three-dimensional CFD models with structured grids, *J. Hydraul. Res.*, *43*, 468–480.

Hardy, R. J., S. N. Lane, R. I. Ferguson, and D. R. Parsons (2007), Emergence of coherent flow structures over a gravel surface: A numerical experiment, *Water Resour. Res.*, *43*, W03422, doi:10.1029/2006WR004936.

Head, M. R., and P. Bandyopadhyay (1981), New aspects of turbulent boundary layer structure, *J. Fluid Mech.*, *107*, 297–338, doi:10.1017/S0022112081001791.

Huang, H., D. Dabiri, and M. Gharib (1997), On errors of digital particle image velocimetry, *Meas. Sci. Technol.*, *8*, 1427–1440, doi:10.1088/0957-0233/8/12/007.

Hunt, J. C. R., C. J. Abell, J. A. Peterka, and H. Woo (1978), Kinematic studies of the flow around free or surface mounted obstacles: Applying topology to flow visualization, *J. Fluid Mech.*, *86*, 179–200, doi:10.1017/S0022112078001068.

Imamoto, H., and T. Ishigaki (1986a), The three dimensional structure of turbulent shear flow in an open channel, paper presented at Fifth Congress of the Asian and Pacific Regional Division of the International Association for Hydraulic Research, Seoul.

Imamoto, H., and T. Ishigaki (1986b), Visualization of longitudinal eddies in an open channel flow, in *Flow Visualization IV: Proceedings of the Fourth International Symposium on Flow Visualization*, edited by C. Veret, pp. 333–337, Hemisphere, Washington, D.C.

Jackson, R. G. (1976), Sedimentological and fluid-dynamic implications of the turbulent bursting phenomenon in geophysical flows, *J. Fluid Mech.*, *77*, 531–560.

Kim, K. T., S. J. Kline, and W. C. Reynolds (1971), The production of turbulence near a smooth wall in a turbulent boundary layer, *J. Fluid Mech.*, *50*, 133–147, doi:10.1017/S0022112071002490.

Kirchner, J. W., W. E. Dietrich, F. Iseya, and H. Ikeda (1990), The variability of critical shear stress, friction angle, and grain protrusion in water-worked sediments, *Sedimentology*, *37*, 647–672, doi:10.1111/j.1365-3091.1990.tb00627.x.

Kirkbride, A. D. (1993), Observations of the influence of bed roughness on turbulence structure in depth-limited flows over gravel beds, in *Turbulence: Perspectives on Flow and Sediment Transport*, edited by N. J. Clifford, J. R. French, and J. Hardisty, pp. 185–196, John Wiley, Chichester, U. K.

Klaven, A. B. (1966), Investigation of the flow turbulent structure (in Russian), *Trans. State Hydrol. Inst.*, *136*, 65–76.

Klaven, A. B., and Z. D. Kopaliani (1973), Laboratory investigations of the kinematic structure of turbulent flow over a rough bed (in Russian), *Trans. State Hydrol. Inst.*, *209*, 67–90.

Komori, S., H. Ueda, F. Ogino, and T. Mizushina (1982), Turbulence structure and transport mechanism at the free surface in an open channel flow, *Int. J. Heat Mass Transfer*, *25*, 513–521, doi:10.1016/0017-9310(82)90054-0.

Kostaschuk, R. A. (2000), A field study of turbulence and sediment dynamics over subaqueous dunes with flow separation, *Sedimentology*, *47*, 519–531, doi:10.1046/j.1365-3091.2000.00303.x.

Krogstad, P. Å., R. A. Antonia, and W. B. Browne (1992), Comparison between rough and smooth-wall turbulent boundary layers, *J. Fluid Mech.*, *245*, 599–617, doi:10.1017/S0022112092000594.

Labat, D., R. Ababou, and A. Mangin (2000), Rainfall-runoff relations for karstic springs. Part II: Continuous wavelet and discrete orthogonal multiresolution analyses, *J. Hydrol.*, *238*, 149–178, doi:10.1016/S0022-1694(00)00322-X.

Lacey, R. W. J., P. Legendre, and A. G. Roy (2007), Spatial scale partitioning of in situ turbulent flow data over a pebble cluster in a gravel-bed river, *Water Resour. Res.*, *43*, W03416, doi:10.1029/2006WR005044.

Lane, S. N., R. J. Hardy, L. Elliott, and D. B. Ingham (2004), Numerical modeling of flow processes over gravelly surfaces using structured grids and a numerical porosity treatment, *Water Resour. Res.*, *40*, W01302, doi:10.1029/2002WR001934.

Lapointe, M. (1992), Burst-like sediment suspension events in a sand bed river, *Earth Surf. Processes Landforms*, *17*, 253–270, doi:10.1002/esp.3290170305.

Lawless, M. R. (2004), Junction flow systems: Mechanics and implications for natural flows, Ph.D. thesis, Univ. of Leeds, Leeds, U. K.

Lawless, M. R., and A. Robert (2001), Scales of boundary resistance in coarse-grained channels: Turbulent velocity profiles and implications, *Geomorphology*, *39*, 221–238, doi:10.1016/S0169-555X(01)00029-0.

Levi, E. (1983), A universal Strouhal law, *J. Eng. Mech.*, *109*, 718–727.
Levi, E. (1991), Vortices in hydraulics, *J. Hydraul. Eng.*, *117*, 399–413, doi:10.1061/(ASCE)0733-9429(1991)117:4(399).
Liandrat, J., and F. Moret-Bailly (1990), The wavelet transform: Some applications to fluid dynamics and turbulence, *Eur. J. Mech. BFluids*, *9*, 1–19.
Lu, S. S., and W. W. Willmarth (1973), Measurements of structure of Reynolds stress in a turbulent boundary layer, *J. Fluid Mech.*, *60*, 481–511, doi:10.1017/S0022112073000315.
Müller, A., and A. Gyr (1982), Visualisation of the mixing layer behind dunes, in *Mechanics of Sediment Transport*, edited by B. M. Summer and A. Müller, pp. 41–45, A. A. Balkema, Rotterdam, Netherlands.
Müller, A., and A. Gyr (1986), On the vortex formation in the mixing layer behind dunes, *J. Hydraul. Res.*, *24*, 359–375.
Nelson, J. M., and J. D. Smith (1989), Mechanics of flow over ripples and dunes, *J. Geophys. Res.*, *94*, 8146–8162, doi:10.1029/JC094iC06p08146.
Nelson, J. M., R. L. Shreve, S. R. McLean, and T. G. Drake (1995), Role of near-bed turbulence structure in bed load transport and bed form mechanics, *Water Resour. Res.*, *31*, 2071–2086, doi:10.1029/95WR00976.
Nezu, I., and H. Nakagawa (1993), *Turbulence in Open Channel Flows*, A. A. Balkema, Rotterdam, Netherlands.
Nezu, I., and W. Rodi (1985), Experimental study of secondary currents in open channel flow, paper presented at 21st IAHR Congress, Int. Assoc. of Hydraul. Res., Melbourne, Victoria, Australia.
Nikora, V. I., and D. G. Goring (1999), Are weakly mobile-bed flows a special class of wall-bounded flows?, paper presented at the 28th Congress of the International Association for Hydraulic Research, Graz, Austria, 22–27 Aug.
Nikora, V. I., and G. M. Smart (1997), Turbulence characteristics of New Zealand gravel-bed rivers, *J. Hydraul. Eng.*, *123*, 764–773, doi:10.1061/(ASCE)0733-9429(1997)123:9(764).
Nowell, A. R. M., and M. Church (1979), Turbulent flow in a depth limited boundary layer, *J. Geophys. Res.*, *84*, 4816–4824, doi:10.1029/JC084iC08p04816.
Nychas, S. G., H. C. Hershey, and R. S. Brodkey (1973), A visual study of turbulent shear flow, *J. Fluid Mech.*, *61*, 513–540, doi:10.1017/S0022112073000844.
Rashidi, M., and S. Banerjee (1988), Turbulence structure in free-surface channel flow, *Phys. Fluids*, *31*, 2491–2503, doi:10.1063/1.866603.
Robert, A., A. G. Roy, and B. De Serres (1992), Changes in velocity profiles at roughness transitions in coarse grained channels, *Sedimentology*, *39*, 725–735, doi:10.1111/j.1365-3091.1992.tb02149.x.
Robert, A., A. G. Roy, and B. De Serres (1993), Space-time correlations of velocity measurements at a roughness transition in a gravel-bed river, in *Turbulence: Perspectives on Flow and Sediment Transport*, edited by N. J. Clifford et al., pp. 165–184, John Wiley, Chichester, U. K.
Rood, K. M., and E. J. Hickin (1989), Suspended sediment concentration in relation to surface-flow structure in Squamish River estuary, southwestern British Columbia, *Can. J. Earth Sci.*, *26*, 2172–2176.
Roy, A. G., T. Buffin-Bélanger, and S. Deland (1996), Scales of turbulent coherent flow structures in a gravel bed river, in *Coherent Flow Structure in Open Channels*, edited by P. J. Ashworth et al., pp. 147–164, John Wiley, Hoboken, N. J.
Roy, A. G., T. Buffin-Bélanger, H. Lamarre, and A. D. Kirkbride (2004), Size, shape and dynamics of large-scale turbulent flow structures in a gravel-bed river, *J. Fluid Mech.*, *500*, 1–27, doi:10.1017/S0022112003006396.
Shen, C., and U. Lemmin (1999), Application of an acoustic particle flux profiler in particle-laden open-channel flow, *J. Hydraul. Res.*, *37*, 407–419.
Shvidchenko, A., and G. Pender (2001), Macroturbulent structure of open-channel flow over gravely beds, *Water Resour. Res.*, *37*, 709–719, doi:10.1029/2000WR900280.
Simpson, R. L. (1989), Turbulent boundary layer separation, *Annu. Rev. Fluid Mech.*, *21*, 205–234, doi:10.1146/annurev.fl.21.010189.001225.
Smith, C. R. (1996), Coherent flow structures in smooth-wall turbulent boundary layers: Facts, mechanisms and speculation, in *Coherent Flow Structures in Open Channels*, edited by P. J. Ashworth et al., pp. 1–40, John Wiley, Hoboken, N. J.
Smith, C. R., J. D. A. Walker, A. H. Haidari, and U. Sobrun (1991), On the dynamics of near-wall turbulence, *Philos. Trans. R. Soc. London, Ser. A*, *336*(1641), 131–175.
Sukhodolov, A. N., and B. L. Rhoads (2001), Field investigation of three dimensional flow structure at stream confluences, *Water Resour. Res.*, *37*, 2411–2424, doi:10.1029/2001WR000317.
Talmon, A. M., J. M. G. Kunen, and G. Oooms (1986), Simultaneous flow visualization and Reynolds stress measurement in a turbulent boundary layer, *J. Fluid Mech.*, *163*, 459–478, doi:10.1017/S0022112086002380.
Tennekes, H., and J. L. Lumley (1972), *A First Course in Turbulence*, MIT Press, Cambridge, Mass.
Torrence, C., and G. P. Compo (1998), A practical guide to wavelet analysis, *Bull. Am. Meteorol. Soc.*, *79*, 61–78, doi:10.1175/1520-0477(1998)079<0061:APGTWA>2.0.CO;2.
Velikanov, M. A. (1949), *Dynamics of Alluvial Flows* (in Russian), Gidrometeoizdat, Leningrad, Russia.
Westerweel, J. (1997), Fundamental of digital particle image velocimetry, *Meas. Sci. Technol.*, *8*, 1379–1392, doi:10.1088/0957-0233/8/12/002.
Wiberg, P. L., and J. D. Smith (1991), Velocity distribution and bed roughness in high-gradient streams, *Water Resour. Res.*, *27*, 825–838, doi:10.1029/90WR02770.
Wilbert, C., and M. Gharib (1991), Digital particle image velocimetry, *Exp. Fluids*, *10*, 181–193.
Yalin, M. S. (1992), *River Mechanics*, 219 pp., Pergamon Press, Oxford, U. K.
Zaitsev, N. I. (1984), Large-scale structure of turbulent flow in a rectangular flume (in Russian), *Trans. State Hydrol. Inst.*, *318*, 3–17.

J. L. Best, Department of Geology, University of Illinois at Urbana-Champaign, 1301 West Green Street, Urbana, IL 61801, USA.

P. E. Carbonneau, R. J. Hardy, and S. N. Lane, Department of Geography, Durham University, Science Site, South Road, Durham DH1 3LE, UK. (r.j.hardy@durham.ac.uk)